Modeling of heat transfer and fluid flow during gas tungsten arc spot welding of low carbon steel

W. Zhang and G. G. Roy
Department of Material Science and Engineering, Pennsylvania State University, University Park, Pennsylvania 16802

J. W. Elmer
Chemistry and Materials Science Department, Lawrence Livermore National Laboratory, Livermore, California 94551

T. DebRoy[a)]
Department of Material Science and Engineering, Pennsylvania State University, University Park, Pennsylvania 16802

(Received 15 November 2002; accepted 4 December 2002)

The evolution of temperature and velocity fields during gas tungsten arc spot welding of AISI 1005 steel was studied using a transient numerical model. The calculated geometry of the weld fusion zone and heat affected zone and the weld thermal cycles were in good agreement with the corresponding experimental results. Dimensional analysis was used to understand the importance of heat transfer by conduction and convection at various stages of the evolution of the weld pool and the role of various driving forces for convection in the liquid pool. The calculated cooling rates are found to be almost independent of position between the 1073 and 773 K (800 and 500 °C) temperature range, but vary significantly at the onset of solidification at different portions of the weld pool. During solidification, the mushy zone grew significantly with time until the pure liquid region vanished. The solidification rate of the mushy zone/solid interface was shown to increase while the temperature gradient in the mushy zone at this interface was shown to decrease as solidification of the weld pool progressed. Tracking these solidification parameters with time shows that the weld pool solidifies with decreasing interface stability, i.e., with a higher tendency to form dendrites towards the center of the weld. © *2003 American Institute of Physics.*
[DOI: 10.1063/1.1540744]

I. INTRODUCTION

Transient welding conditions are encountered in many everyday welding situations such as weld starts and stops, tack-welding routines, stationary spot welds, and solidifying weld craters. These types of welds behave differently than their moving weld counterparts because the thermal profiles never reach a steady state value. The heating and cooling rates for these welds are often much higher than that of steady state welds, and can lead to solidification cracking and formation of nonequilibrium phases. Therefore it is important to understand how the weld thermal profiles change as a function of time.

Because of the small size of the weld pool, the presence of plasma in the vicinity of the weld pool and the rapid changes of temperature in arc spot welds, physical measurements of important parameters such as temperature and velocity fields, solidification rate, and thermal gradient in the weld pool are extremely difficult. Therefore, in recent decades, numerical calculations of heat transfer and fluid flow have been utilized to understand various weld characteristics that cannot be obtained otherwise.

In a first attempt to model the transient welding processes, Oreper *et al.*[1] studied the evolution of temperature and velocity fields, solidification rate, and thermal gradient using a two-dimensional model. Due to the hardware limitation at that time, a rather crude grid system (typically 18 $\times$20) was used, but the calculations provided useful temperature and velocity fields. Oreper and Szekely[2] used dimensionless analysis and numerical modeling to understand the role of conduction and convection in the weld pool heat transfer for materials with different thermal physical properties. Zacharia *et al.*[3,4] carried out computational and experimental study to investigate the effect of the surface active element (sulfur) on the weld pool geometry. Betram[5] examined the role of the heat and liquid flows on the final solidification microstructure considering the mushy zone behavior. Kim and Na[6] investigated the heat transfer and fluid flow in the weld pool with deformable free surface during pulsed current gas tungsten arc (GTA) welding. More recently, Wang and Tsai[7] investigated the weld pool convection and weld penetration in gas metal arc (GMA) welding. Their study was focused on the effect of surface active elements and the transport of filler droplets into the weld pool.

In summary, the transport phenomena based numerical models have been successful in revealing special features in transient spot welding processes such as the transient nature of the solidification rate.[1,5] However, a detailed analysis of the transient heating and solidification behavior still remains to be undertaken to investigate how the mushy zone region

[a)]Electronic mail: debroy@psu.edu

behaves during heating and solidification and how the solidification front velocity changes with time during spot welding. Such a computationally intensive investigation, requiring the use of very fine grids and very small time steps, has now become practical because of recent advances in the computational hardware and software.

In this study, a transient numerical model was used to provide detailed insight about the nature of heat transfer and fluid flow during GTA stationary spot welding of 1005 steel. Electromagnetic, surface tension, and buoyancy driving forces were considered for the calculation of transient weld pool convection. The weld pool boundary was traced using an enthalpy-porosity technique[8] in a fixed Cartesian coordinate system. For the accuracy of the calculation, a very fine grid system and small time step were used. Verification of the model was performed through comparing the calculated results with metalographic weld cross sections and weld thermal cycles measured by thermocouples. Dimensionless analysis was carried out to understand the heat transfer mechanism and the significance of the various driving forces for the liquid pool convection. The calculated temperature distributions, and heating and cooling rates are useful for understanding phase transformation kinetics. The behavior of the mushy zone, i.e., the solid+liquid two phase region, during heating and cooling was investigated. Results also revealed information about the important solidification parameters R, the solidification rate (m/s), and G, the temperature gradient (K/m) in the mushy zone at the mushy zone/solid front, as a function of time. These data are useful for determining the solidification morphology and the scale of the solidification substructure. This work demonstrates that the application of numerical transport phenomena can significantly add to the quantitative knowledge base in welding and help the welding community in solving practical problems.

II. MATHEMATICAL FORMULATION

During spot welding, the weld temperature and velocity fields are essentially axis-symmetric due to the nature of heat distribution.[1–4] This allows the governing equations to be solved in a two-dimensional (2D) system. However, the calculations presented here for GTA spot welds are carried out in a three-dimensional (3D) Cartesian coordinate system since our heat transfer and fluid flow model is also used for the calculation of moving heat source welding, which is a 3D problem. Therefore, in the following formulation, all the governing equations are presented in their 3D form.

A. Governing equations

An incompressible, laminar, and Newtonian liquid flow is assumed in the weld pool. Thus the circulation of liquid metal in the weld pool can be represented by the following momentum equation:[9]

$$\rho\frac{\partial u_j}{\partial t}+\rho\frac{\partial(u_i u_j)}{\partial x_i}=\frac{\partial}{\partial x_i}\left(\mu\frac{\partial u_j}{\partial x_i}\right)+S_j, \tag{1}$$

where ρ is the density, t is the time, x_i is the distance along the i ($i=1$, 2, and 3) direction, u_j is the velocity component along the j direction, μ is the viscosity, and S_j is the source term for the jth momentum equation and is given as

$$S_j=-\frac{\partial p}{\partial x_j}+\frac{\partial}{\partial x_i}\left(\mu\frac{\partial u_j}{\partial x_j}\right)-C\left(\frac{(1-f_L)^2}{f_L^3+B}\right)u_j+\mathrm{Se}_j+\mathrm{Sb}_j, \tag{2}$$

where p represents pressure. In Eq. (2), the first term on the right-hand side (RHS) is the pressure gradient.[9] The second term is the viscosity term arising from casting the momentum equation into a general form.[10] The third term represents the frictional dissipation in the mushy zone according to the Carman–Kozeny equation for flow through a porous media,[11,12] where f_L is the liquid fraction, B is a very small computational constant introduced to avoid division by zero, and C is a constant accounting for the mushy zone morphology (a value of 1.6×10^4 was used in the present study[13]). The fourth and fifth terms, Se_j and Sb_j, correspond to the electromagnetic and buoyancy source terms, respectively. Details about the calculation of the electromagnetic and buoyancy source terms are available in the literature.[13,14]

The following continuity equation is solved in conjunction with the momentum equation to obtain the pressure field.

$$\frac{\partial(\rho u_i)}{\partial x_i}=0. \tag{3}$$

In order to trace the weld pool liquid/solid interface, i.e., the phase change, the total enthalpy H is represented by a sum of sensible heat h and latent heat content ΔH, i.e., $H=h+\Delta H$.[11,12] The sensible heat h is expressed as $h=\int C_p dT$, where C_p is the specific heat, and T is the temperature. The latent heat content ΔH is given as $\Delta H=f_L L$, where L is the latent heat of fusion. The liquid fraction f_L is assumed to vary linearly with temperature:[13]

$$f_L=\begin{cases}1, & T>T_L\\ \dfrac{T-T_S}{T_L-T_S}, & T_S\leqslant T\leqslant T_L,\\ 0, & T<T_S\end{cases} \tag{4}$$

where T_L and T_S are the liquidus and solidus temperature, respectively. Thus the thermal energy transportation in the weld workpiece can be expressed by the following modified energy equation:

$$\rho\frac{\partial h}{\partial t}+\rho\frac{\partial(u_i h)}{\partial x_i}=\frac{\partial}{\partial x_i}\left(\frac{k}{C_p}\frac{\partial h}{\partial x_i}\right)+S_h, \tag{5}$$

where k is the thermal conductivity. The source term S_h is due to the latent heat content and is given as

$$S_h=-\rho\frac{\partial(\Delta H)}{\partial t}-\rho\frac{\partial(u_i\Delta H)}{\partial x_i}. \tag{6}$$

B. Boundary conditions

A 3D Cartesian coordinate system is used in the calculation, while only half of the workpiece is considered since the weld is symmetrical about the weld center line. Figure 1

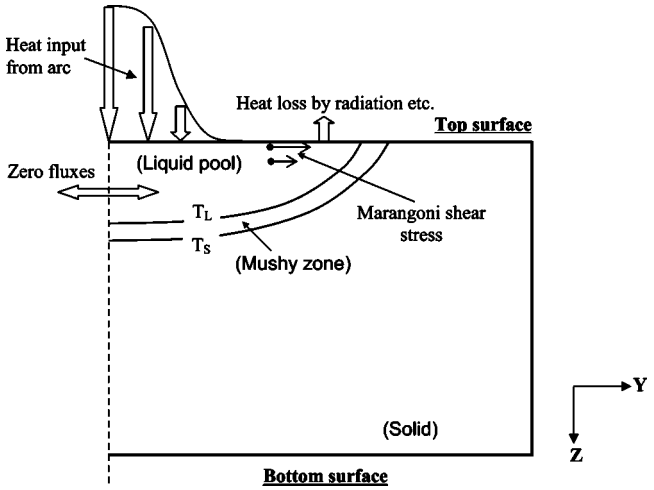

FIG. 1. A schematic plot of the weld cross section showing boundary conditions used in the calculation.

is a schematic plot showing the boundary conditions. These boundary conditions are further discussed as follows.

1. Top surface

The weld top surface is assumed to be flat. The velocity boundary condition is given as[13]

$$\mu\frac{\partial u}{\partial z}=f_L\frac{d\gamma}{dT}\frac{\partial T}{\partial x},$$

$$\mu\frac{\partial v}{\partial z}=f_L\frac{d\gamma}{dT}\frac{\partial T}{\partial y}, \tag{7}$$

$$w=0,$$

where u, v, and w are the velocity components along the x, y, and z directions, respectively, and $d\gamma/dT$ is the temperature coefficient of surface tension. As shown in this equation, the u and v velocities are determined from the Marangoni effect. The w velocity is equal to zero since there is no outward flow at the pool top surface.

The heat flux at the top surface is given as

$$k\left.\frac{\partial T}{\partial z}\right|_{\text{top}}=\frac{fQ\eta}{r_b^2}\exp\left(-\frac{f(x^2+y^2)}{r_b^2}\right)-\sigma\varepsilon(T^4-T_a^4)-h_c(T-T_a), \tag{8}$$

where r_b is the heat distribution parameter, f is the power distribution factor, Q is the total arc power, η is the power efficiency, σ is the Stefan–Boltzmann constant, h_c is the heat transfer coefficient, and T_a is the ambient temperature. In Eq. (8), the first term on the RHS is the heat input from the heat source, defined by a Gaussian heat distribution. The second and third terms represent the heat loss by radiation and convection, respectively.

2. Symmetric surface

The boundary conditions are defined as zero flux across the symmetric surface as

$$\frac{\partial u}{\partial y}=0,\quad v=0,\quad \frac{\partial w}{\partial y}=0, \tag{9}$$

$$\frac{\partial h}{\partial y}=0. \tag{10}$$

3. Other surfaces

At all other surfaces, temperatures are set at ambient temperature (T_a) and the velocities are set to be zero.

C. Discretization of governing equations

The detailed method of discretizing the governing equations is available in the literature.[13] A brief description is presented here to highlight the salient features. The governing equations are discretized using the control volume method,[10] where the computational domain is divided into small rectangular control volumes. A scalar grid point is located at the center of each control volume, storing the values of scalar variables such as pressure and enthalpy. Velocity components are stored at separate locations, staggered with respect to scalar locations, to ensure the stability of numerical calculation. Thus the control volumes for scalars are different from those for the vectors. Discretized equations for a variable are formulated by integrating the corresponding governing equation over the control volumes. The final discretized equation takes the following form:[10]

$$a_P\phi_P=\sum_{\text{nb}}(a_{\text{nb}}\phi_{\text{nb}})+a_P^0\phi_P^0+S_U\Delta V, \tag{11}$$

where subscript P represents a given grid point, while subscript nb represents the neighbors of the given grid point P,

TABLE I. Physical properties of 1005 steel used in the calculation.

Physical property	Value
Liquidus temperature, T_L (K)	1802.0
Solidus temperature, T_S (K)	1779.0
Density of liquid metal, ρ (kg/m^3)	7.2×10^3
Effective viscosity of liquid, μ (kg/m s)	0.1
Thermal conductivity of solid, k_S (J/m s K)	36.4
Effective thermal conductivity of liquid, k_L (J/m s K)	109.2
Specific heat of solid, C_{PS} (J/kg K)	754.0
Specific heat of liquid, C_{PL} (J/kg K)	754.0
Temperature coefficient of surface tension, $d\gamma/dT$ (N/m K)	-0.43×10^{-3}
Coefficient of thermal expansion, β (K^{-1})	1.7×10^{-6}
Magnetic permeability, μ_m (N/A^2)	1.26×10^{-6}

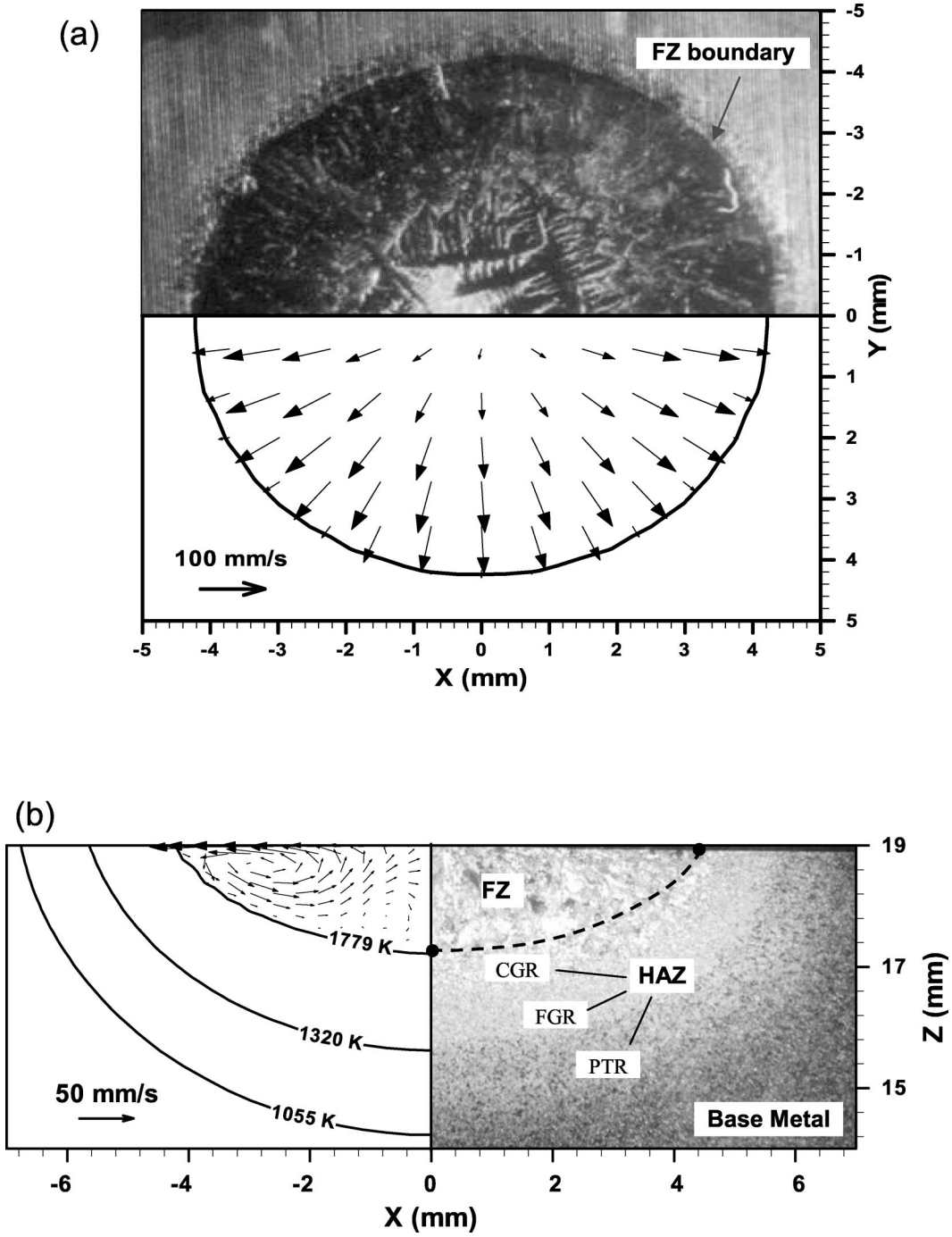

FIG. 2. Comparison between the calculated and measured weld pool geometry. (a) the top surface and (b) the cross section. Welding conditions: arc current=120 A, arc voltage=17.5 V, and arc on time=16 s. Symbols CGR, FGR, and PTR represent the coarse grained region, fine grained region, and partially transformed region, respectively. The HAZ consists of the CGR, FGR, and PTR regions.

ϕ is a general variable such as velocity or enthalpy, a is the coefficient calculated based on the power law scheme, ΔV is the volume of the control volume, a_P^0 and ϕ_P^0 are the coefficient and value of the general variable at the previous time step, respectively. The coefficient a_P is defined as

$$a_P=\sum_{\text{nb}} a_{\text{nb}}+a_P^0-S_P\Delta V. \tag{12}$$

The terms S_U and S_P are used in the source term linearization as

$$S=S_U+S_P\phi_P. \tag{13}$$

D. Grid spacings and time steps

Accurate calculation of weld temperature and velocity fields, solidification rates, and the temperature gradients requires the use of a very fine grid system and small time steps. A typical grid system used in the present study contained $130\times65\times60$ grid points, and the corresponding computational domain had dimensions of 64 mm in length, 32 mm in

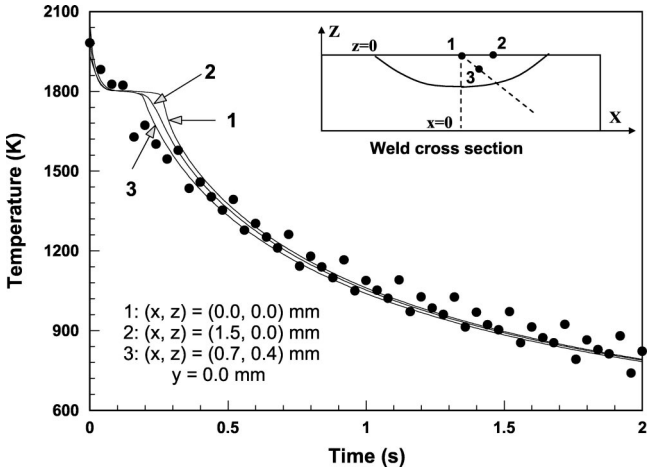

FIG. 3. Comparison between the measured and calculated cooling curves. Welding conditions: arc current = 108 A, arc voltage = 18 V, and arc on time = 10 s. The time zero corresponds to the time when the arc is switched off at $t = 10$ s. The measured cooling curve is represented by the solid dots. The superimposed cooling curves are calculated at several different locations in the weld pool, as shown in the small figure.

width, and 22 mm in depth. Spatially nonuniform grids were used for maximum resolution of variables. A finer grid spacing was used near the heat source. The minimum grid spacings along the x and z directions were about 50 and 20 μm, respectively. The time step used in the cooling part was 1 ms to ensure the accurate calculation of solidification parameters, while the time step used in the heating part was 20 ms to reduce the computational time.

E. Convergence criteria

At each time step, the discretized equations are solved using the SIMPLE algorithm.[10] The calculation proceeds to the next time step if certain convergence criteria are met. In the present study, two convergence criteria are used, i.e., residuals and heat balance.

The residuals for velocities and enthalpy are defined as

$$R = \frac{\sum_{\text{domain}} \left| \frac{\sum_{\text{nb}} (a_{\text{nb}} \phi_{\text{nb}}) + a_P^0 \phi_P^0 + S_U \Delta V}{a_P} - \phi_P \right|}{\sum_{\text{domain}} |\phi_P|}. \quad (14)$$

The residual values should be usually very small when a converged solution is obtained.

The following overall heat balance check provides another criterion for the convergence of the solution.

$$\theta = \left| \frac{\text{net heat input}}{\text{total heat out} + \text{heat accumulation}} \right|. \quad (15)$$

Upon convergence, heat balance ratio θ should be very close to 1.

In the present study, we define the convergence as reached when $R \leqslant 10^{-4}$ and $0.999 \leqslant \theta \leqslant 1.001$. More restrictive convergence conditions do not change the final results while increasing the computational time significantly.

III. SPOT WELDING EXPERIMENTS

AISI 1005 carbon manganese steel in the form of a 10.2 cm diameter cylindrical bar was used for all of the experiments. The composition of the as-received bar was (by wt %): 0.05 C, 0.31 Mn, 0.18 Si, 0.11 Ni, 0.10 Cr, 0.009 P, 0.008 Cu, 0.005 S, $<$0.005 Al, $<$0.005 Nb, $<$0.005 Mo, $<$0.005 Ti, and $<$0.005 V. GTA spot welds were made on steel bars using a 225 A direct constant current welding power supply with electrode negative polarity. The welding electrode was made of W-2%Th measuring 4.7 mm in diameter. High purity (99.999%) helium was used as both the welding and shielding gases. In the welding experiments, both the arc current and voltage were maintained constant at about 110 A and 18 V, respectively. Additional details about the welding procedure are reported in the literature.[15] The physical properties for 1005 steel used in the calculations are listed in Table I.

IV. RESULTS AND DISCUSSION

A. Validation of the transient heat transfer and fluid flow model

In the spot welding experiments, the arc on time was set to more than 10 s, which was long enough to ensure that the weld pool was fully developed. Figures 2(a) and 2(b) show the comparison between the measured and calculated geometry of the fusion zone (FZ) at the weld top surface and vertical cross section, respectively. In these figures, the weld pool boundary, represented by the solidus isotherm (1779 K), was calculated just before the arc was extinguished at $t = 16$ s. The dashed line in Fig. 2(b) corresponds to the experimentally measured fusion line at the weld cross section. As shown in these figures, the calculated geometry of the FZ agrees well with the experimental result.

Three microstructural subregions, namely, the partially transformed region (PTR), the fine grained region (FGR), and the coarse grained region (CGR),[15,16] were observed in the heat affected zone (HAZ) of the weld cross section, as shown in Fig. 2(b). The presence of these phase regions depends on both local thermal cycles and kinetics of phase transformations. In general, the PTR is the region where α-ferrite partially transforms into γ-austenite, while the FGR corresponds to the region where α-ferrite to γ-austenite transformation completes[15] but has not had enough time for γ-austenite grain growth. The A3 (1204 K) and A1 (991 K) temperatures for 1005 steel are normally used to represent FGR/PTR and PTR/base metal boundaries, respectively.[17] However, the calculated isotherms at 1320 and 1055 K matched the size and location of the FGR/PTR and PTR/base metal boundaries better that the A3 and A1 isotherms. These two temperatures, 1320 and 1055 K, are higher than the A3 and A1 temperatures for 1005 steel, indicating that superheating was required for the α-ferrite to γ-austenite transformation under the rapid heating conditions in spot welding.

Figure 3 shows the comparison between the measured and calculated cooling curves. The cooling curve was measured by plunging a thermocouple into the weld pool and switched off the arc at the same time. In this figure, the measured cooling curve is plotted as solid dots, while the

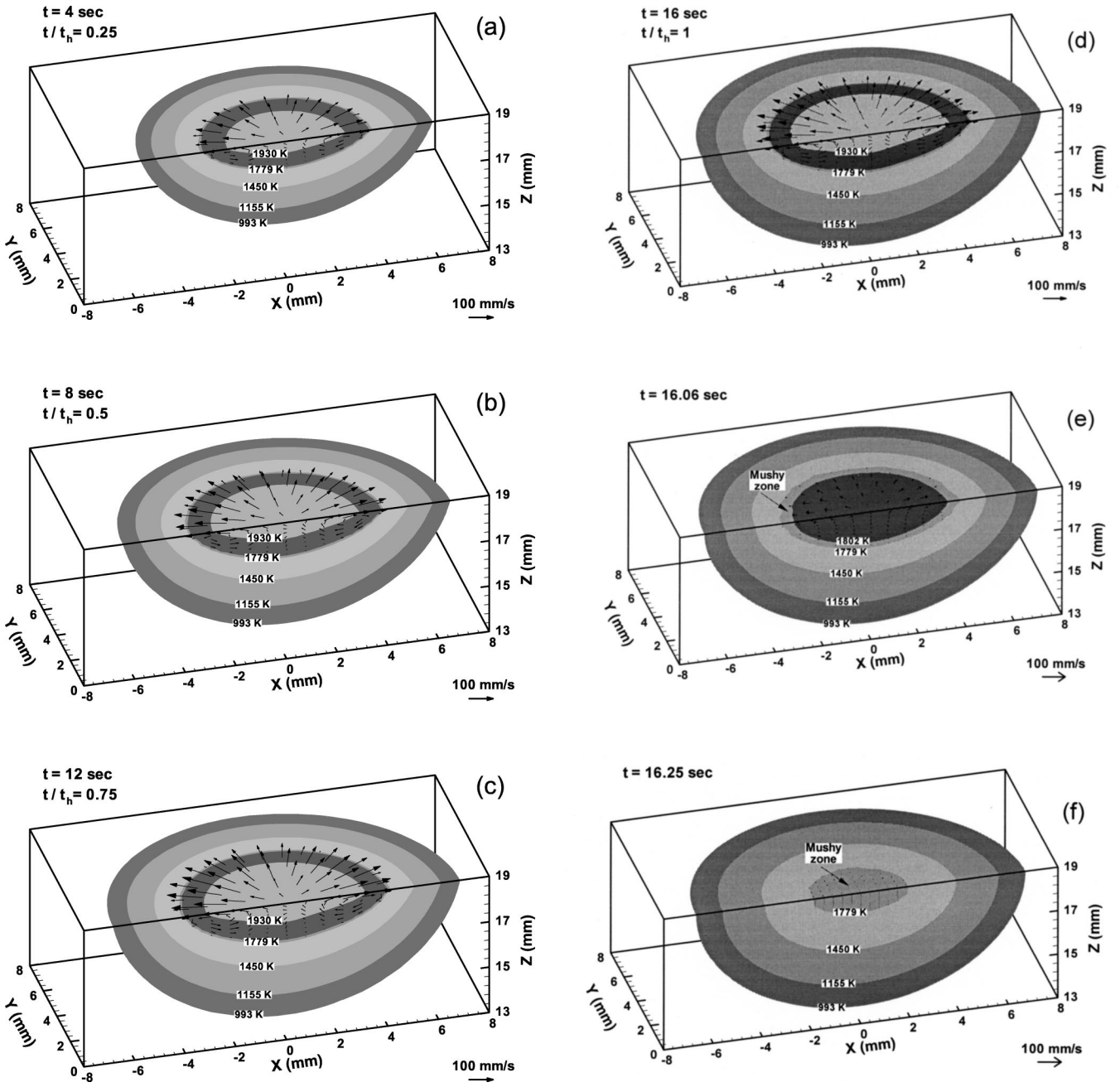

FIG. 4. Evolution of temperature and velocity fields. (a) $t=4$ s; (b) $t=8$ s; (c) $t=12$ s; (d) $t=16$ s; (e) $t=16.06$ s; and (f) $t=16.25$ s. Welding conditions: arc current=120 A, arc voltage=17.5 V, and arc on time $(t_h)=16$ s. (a)–(d) are for heating while (e) and (f) are for cooling of the weld. The velocities are represented by the arrows while the temperatures (K) are represented by the contours.

calculated cooling curves at three different locations in the weld pool are represented by the lines. As shown in Fig. 3, there is a plateau in the calculated cooling curves. In other words, the cooling rate is rather small in this region. This is due to the evolution of the latent heat of fusion, as discussed in the next section. Although the thermocouple data does not capture the temperature plateau, the otherwise good agreement between the computed and the experimental weld pool geometry and cooling curves indicate the validity of the transient heat transfer and fluid flow model.

B. Evolution of temperature and velocity fields

Figure 4 shows the evolution of temperature and velocity fields in the workpiece. For clarity, only a half of the weld is shown. As depicted in this figure, when the arc starts, the arc energy input leads to rapid heating, melting, and the formation of the weld pool. The liquid metal motion in the weld pool is driven mainly by the surface tension and electromagnetic forces and, to a much lesser extent, by the buoyancy force. The relative importance of these driving forces is quantitatively examined in a subsequent section. Because the temperature coefficient of surface tension $d\gamma/dT$ has a negative value, the surface tension force drives the liquid metal from the center to the periphery at the top surface of the weld pool. As a result, the weld pool becomes wide and shallow. When the arc is switched off, the weld pool shrinks very rapidly, as shown in Figs. 4(e) and 4(f). The calculations

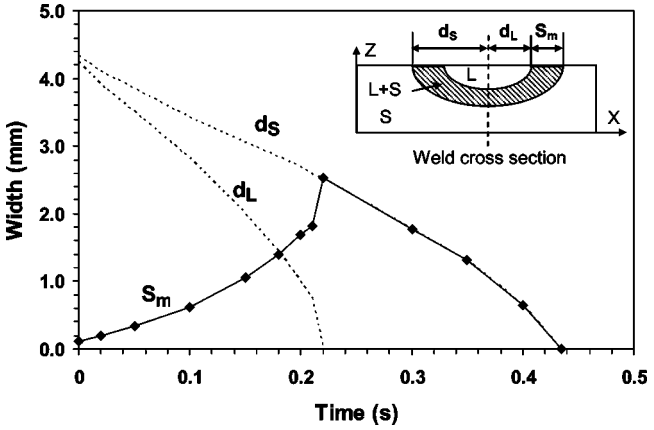

FIG. 5. Evolution of the mushy zone size during solidification. The symbols d_L and d_S are the distances from the weld center to the liquid/mushy zone and mushy zone/solid interfaces at the pool top surface, respectively. The size of the mushy zone, S_m, is defined as the difference between d_S and d_L, as shown in the small figure.

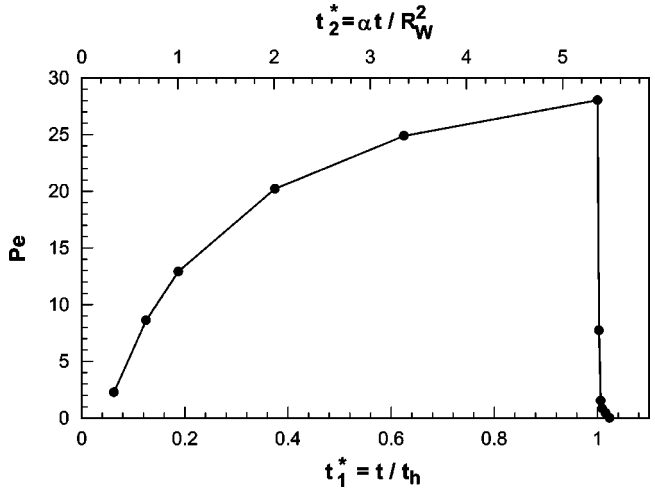

FIG. 7. Peclet number as a function of two dimensionless times. Weld conditions are the same as those in Fig. 3.

show that the entire weld pool solidifies in about 435 ms after the arc is turned off. Figures 4(e) and 4(f) show a dramatic drop in the liquid velocity as the pool solidifies. This is due to the fact that as the arc is turned off, the electromagnetic force is discontinued. The surface tension force also decreases rapidly as the temperature gradient at the pool top surface drops significantly. Thus the liquid metal motion is maintained mainly by inertia. Furthermore, the rapid shrinkage of the weld pool restricts the flow. As a result, the flow diminishes rapidly during solidification. However, although the velocities decay quite rapidly, the average velocity at 350 ms after the starting of solidification is still about 1 mm/s. Therefore most of the weld pool solidification takes place from an essentially circulating melt. However, the mixing of the liquid diminishes as solidification proceeds.

In the present study, the mushy zone, i.e., the solid + liquid two-phase region, is determined as the region having temperatures between the solidus and liquidus isotherms. As shown in Figs. 4(a)–4(d), the size of the mushy zone is very small during heating. This is due to the large temperature gradient in the weld. Figure 5 shows the evolution of the mushy zone size during solidification. As shown in this figure, the mushy zone expands initially and the maximum size of the mushy zone is reached when the pure liquid region diminishes. The size of the mushy zone then decreases as solidification proceeds further. The initial expansion of the mushy zone size could be explained by considering the effect of the latent heat of fusion. The energy conservation equation for a unit cell in the liquid pool is expressed as

$$H_{\text{loss}} = -C_P \frac{dT}{dt} - L \frac{df_L}{dt}, \tag{16}$$

where H_{loss} is the heat loss rate per unit mass, and C_P, T, t, L, and f_L have been defined earlier. The first and second terms in the right-hand side of Eq. (16) account for the heat loss due to the decrease of temperature and latent heat content, respectively. When the temperature is higher than the liquidus temperature, the heat loss is accompanied by the decrease in temperature. As the temperature drops between the liquidus and solidus temperatures, the heat loss now originates primarily from the release of the latent heat of fusion, and the temperature decreases slowly in this temperature range. In other words, the cooling rate defined by dT/dt is small between the liquidus and solidus temperature range, as indicated by the plateau in the calculated cooling curves in Fig. 3. As a result of heat loss during the initial period of solidification, the pure liquid region vanishes at the early stage of solidification and leaves the weld pool occupied by the mushy region. The evolution of the mushy zone during solidification is demonstrated more clearly in Fig. 6. As shown in this figure, the temperature gradient in the liquid pool drops rapidly. The pure liquid region disappears in about 220 ms after the solidification starts, and the mushy zone exits for about another 215 ms before the weld pool solidifies completely. The existence of a mushy pool is a unique feature of the solidification during spot welding and has a significant effect on the final solidified microstructure.[5]

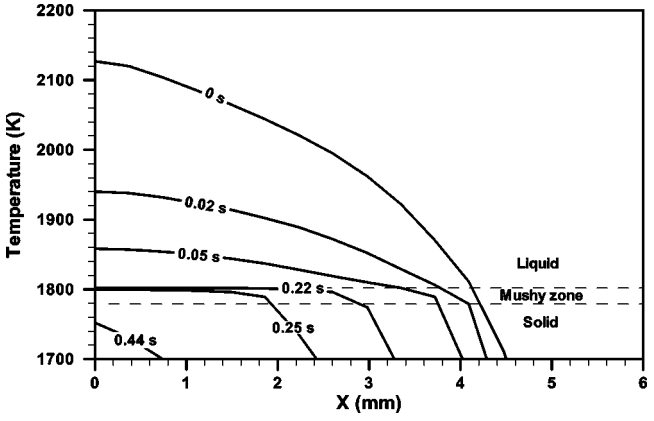

FIG. 6. Distribution of temperature at the pool top surface at various solidification times. Time equal to zero corresponds to the time when the arc is switched off, i.e., start of the solidification.

TABLE II. Dimensionless numbers calculated in the weld pool just before the arc was extinguished.

Dimensionless number	Description	Value
Grashof number, Gr	Ratio of buoyancy to viscous force	62.0
Magnetic Reynolds number, Rm	Ratio of electromagnetic force to viscous force	7.4×10^4
Surface tension Reynolds number, Ma	Ratio of surface tension force to viscous force	1.3×10^5

C. Estimation of scaling and order of magnitude using dimensionless numbers

1. Relative importance of heat transfer by conduction and convection in the weld pool

The Peclet number, Pe, is defined by Eq. (17). This number is used to evaluate the relative importance of heat transfer by conduction and convection in the weld pool.

$$\mathrm{Pe}=\frac{u_R\rho C_p L_R}{k}, \tag{17}$$

where u_R and L_R are the typical velocity and characteristic length of the weld pool, respectively, and the symbols ρ, C_p, and k have been defined earlier. As shown in Fig. 4, the outward flow driven by the surface tension force is dominant in the liquid metal circulation and has significant effect on modifying the weld pool shape. Hence, u_R is taken as the average u velocity and L_R is taken as the pool radius at the top surface of the weld pool.

For spot welding, the value of the Peclet number is a function of time since both u_R and L_R depend on time. From the dimensional analysis, two dimensionless times, t_1^* and t_2^*, are defined as

$$t_1^*=\frac{t}{t_h}, \tag{18}$$

$$t_2^*=\frac{\alpha t}{R_W^2}, \tag{19}$$

where t_h is the arc duration, α is the thermal diffusivity of liquid metal ($\alpha=\rho/kC_P$), and R_W is the weld pool radius at steady state (a value of 4.5 mm used). As shown in Eqs. (18) and (19), t_1^* represents the ratio between the actual time and the heating time, while t_2^* defines the extent of heat transfer by conduction in the weld pool. Figure 7 shows the calculated Peclet number as a function of the two dimensionless times. As shown in this figure, the Peclet number progressively increases during the growth of the weld pool and decreases dramatically during the solidification of the weld pool. This behavior indicates that at the early stage of heating, the heat transfer by conduction is comparable to that by convection in the weld pool. As the weld pool grows, the heat transfer by convection becomes increasingly important in the weld pool. Thus convection plays a dominant role in modifying the shape of the weld pool when the pool is fully developed. After the arc is switched off, the heat transfer by conduction soon becomes more important than that by convection during solidification due to the rapidly diminished velocity.

2. Relative importance of driving forces in the weld pool

The driving forces for the flow in the weld pool considered in the present study include surface tension, electromagnetic, and buoyancy forces. The relative importance of these driving forces can be estimated using several dimensionless numbers, as indicated in Eqs. (20a)–(20c).[2,18]

The ratio of buoyancy force to viscous force is determined by the Grashof number:

$$\mathrm{Gr}=\frac{g\beta L_B^3\Delta T\rho^2}{\mu^2}, \tag{20a}$$

where g is the gravitational acceleration, β is the thermal expansion coefficient, ΔT is the temperature difference between the peak pool temperature and solidus temperature (a value of 350 K is used), and L_B is a characteristic length for the buoyancy force in the liquid pool, and is approximated by one-eighth of the pool radius.[18]

The magnetic Reynolds number defines the ratio of electromagnetic force to viscous force, and is expressed as

$$\mathrm{Rm}=\frac{\rho\mu_m I^2}{4\pi^2\mu^2}, \tag{20b}$$

where μ_m is magnetic permeability.

The surface tension Reynolds number is used to describe the ratio of surface tension gradient force to viscous force, and is calculated as

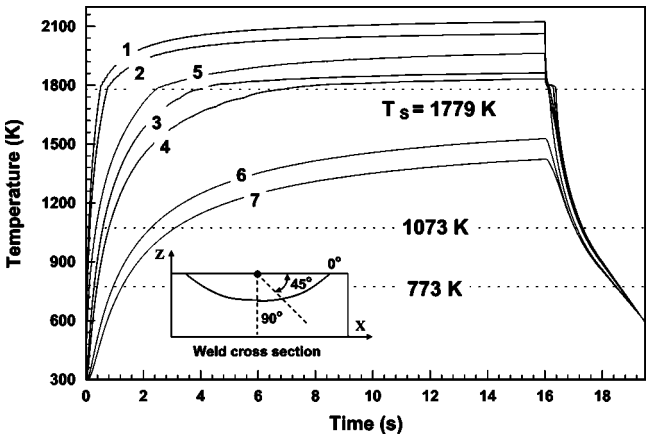

FIG. 8. Weld thermal cycles at different locations. Distance from the weld center: 1: 0.0 mm; 2: 1.5 mm at 0°; 3: 1.5 mm at 45°; 4: 1.5 mm at 90°; 5: 3.0 mm at 0°; 6: 3.0 mm at 45°; and 7: 3.0 mm at 90°, as shown in the small figure. Welding conditions are the same as those in Fig. 3.

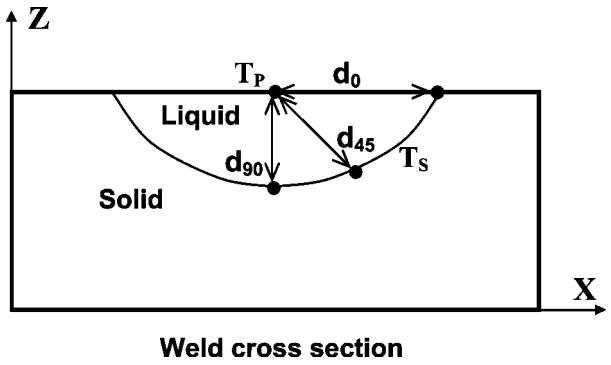

FIG. 9. Schematic plot showing the calculation of average temperature gradient in the weld pool. The symbols d_0, d_{45}, and d_{90} are the distances from the weld center to the pool boundary along 0°, 45°, and 90° planes, respectively.

$$\mathrm{Ma}=\frac{\rho L_R \Delta T\left|\frac{d\gamma}{dT}\right|}{\mu^2}. \tag{20c}$$

Using the physical properties listed in Table I, the calculated dimensionless numbers at $t=16$ s (i.e., just before the arc is switched off) are summarized in Table II. The relative importance of the primary driving forces, i.e., surface tension, electromagnetic and buoyancy force, can thus be judged by the combination of these dimensionless numbers. For example, the ratio of surface tension force to buoyancy force is expressed as

$$R_{S/B}=\frac{\mathrm{Ma}}{\mathrm{Gr}}, \tag{21a}$$

while the ratio of electromagnetic force to buoyancy force is given by

$$R_{M/B}=\frac{R_m}{\mathrm{Gr}}. \tag{21b}$$

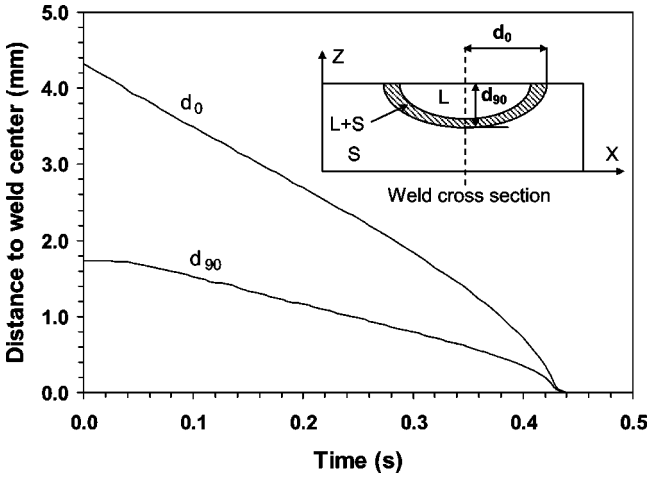

FIG. 10. Distance between the mushy zone/solid front and weld center as a function of solidification time. The distances d_0 and d_{90} are measured along the 0° and 90° planes, respectively, as shown in the small figure. The time zero corresponds to the time when the arc is switched off at $t=16$ s.

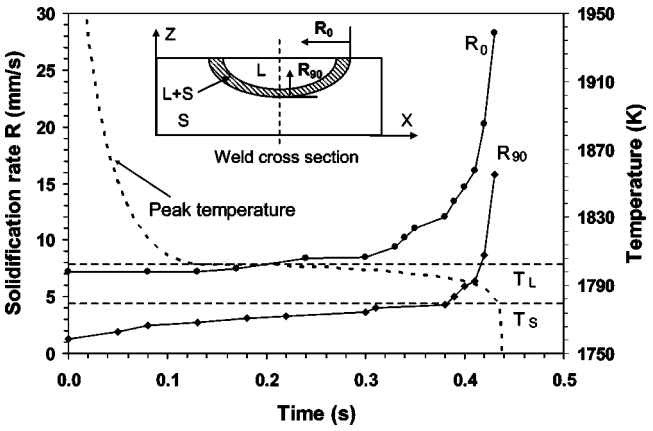

FIG. 11. Solidification rate, R, as a function of time. The growth rates R_0 and R_{90} are calculated along the 0° and 90° planes, respectively, as shown in the small figure. The superimposed dashed curve indicates the peak temperature at the weld pool center versus time data.

Based on the values listed in Table II, $R_{S/B}$ is equal to 2.1×10^3, and $R_{M/B}$ is equal to 1.2×10^3. Therefore we expect that the liquid flow is mainly driven by the surface tension and electromagnetic forces, and to a much less extent, by the buoyancy force.

3. Order of magnitude of maximum velocity in the weld pool

Since the surface tension force is the dominant driving force for convection in the weld pool, the order of magnitude the maximum velocity can be approximated by[19]

$$u_m^{3/2}\approx\frac{d\gamma}{dT}\frac{dT}{dR_W}\frac{R_W^{1/2}}{0.664\rho^{1/2}\mu^{1/2}}, \tag{22}$$

where dT/dR_W is the average temperature gradient in the weld pool (8.5×10^3 K/m). Using Eq. (22), the maximum velocity is estimated to be of the order of 80 mm/s. This value is in good agreement with that calculated using the 3D transient heat transfer and fluid flow model, where the maximum velocity at $t=16$ s was found to be about 100 mm/s.

The foregoing dimensional analysis provided insights about the weld pool development during spot welding. The role of conduction and convection on heat transfer in the weld pool, the relative importance of driving forces for liquid metal convection, the order of magnitude of the velocity

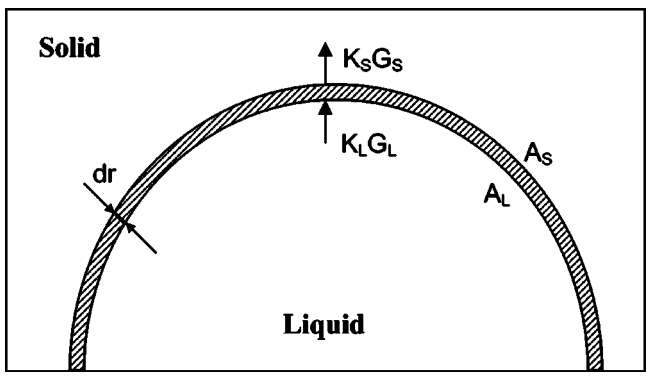

FIG. 12. Schematic plot showing the solidification of a thin liquid shell.

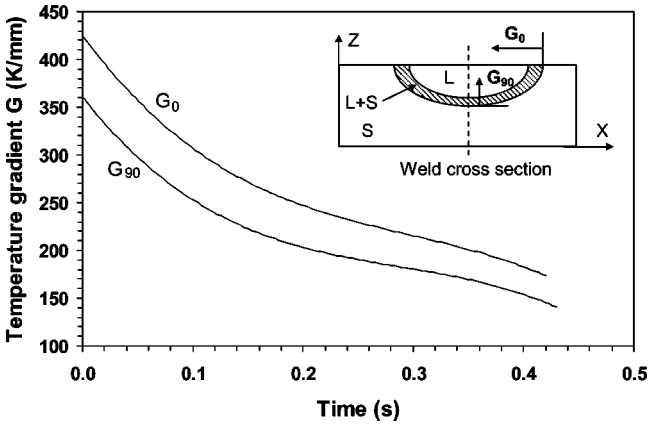

FIG. 13. Evolution of the temperature gradient, G, calculated in the mushy zone at the mushy zone/solid interface at the 0° and 90° planes during solidification.

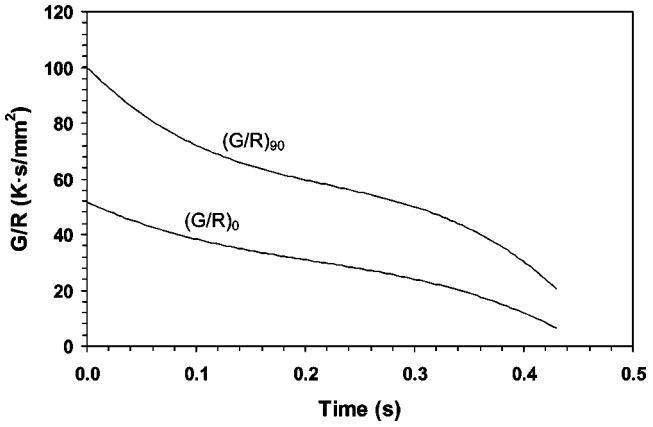

FIG. 14. Calculated solidification parameter G/R at the 0° and 90° planes.

driven by the surface tension force, and the weld pool shape could be estimated using several dimensionless numbers. It should be noted that these order of magnitude analyses cannot provide accurate and detailed information on the spot welding processes, which requires numerical calculation with a very fine grid system and small time step.

D. Weld thermal cycles during spot welding

Figure 8 shows the calculated thermal cycles at different locations in the weldment. As shown in this figure, the monitoring locations 2, 3, and 4 are of the same 1.5 mm distance from the weld center but at 0°, 45°, and 90° planes, respectively. Similarly, monitoring locations 5, 6, and 7 are located along 0°, 45°, and 90° planes, respectively, with a distance of 3 mm from the weld center. For locations of the same distance from the weld center, the temperatures at the 0° plane, such as curve 2, are the highest, while those at the 90° plane, such as curve 4 are the lowest. This variation is mainly due to the effect of the wide and shallow pool geometry resulting from the surface tension driven flow, which increases the temperature gradient along the 90° plane with respect to the 0° plane. As shown in Fig. 9, the average temperature gradient, $\overline{G_a}$, of the weld pool along a given plane is defined as

$$\overline{G_a}=\frac{T_P-T_S}{d}, \tag{23}$$

where T_p is the peak temperature, T_S is the solidus temperature, and d is the distance between the weld center and pool boundary at the given plane. Since d is maximum at the 0° plane and minimum at the 90° plane, the value of $\overline{G_a}$ at the 90° location is the highest while that at the 0° plane is the lowest. For locations of the same distance to the weld center, the higher the average temperature gradient, the lower the temperature. Therefore the temperatures at the 0° plane are the highest and those at the 90° plane are the lowest.

Figure 8 also indicates that the peak temperatures and heating rates at different locations vary significantly. Similarly, the cooling rates vary with position at high temperatures above the melting point. However, as the weld metal cools, the spatial variation of cooling rates decreases. In the 1073–773 K (800–500 °C) range, the cooling rate is almost independent of position, as shown in Figs. 3 and 8. This is due to the nearly constant outward heat loss from all locations of the weld. Thus in steels, where much of the final microstructure is determined by the cooling rate through this temperature range, the spatial variation of microstructures is expected to be small. However, there are certain alloys where a small change in the cooling rate may result in significant difference in the final microstructure.[20] In such cases, the spatial variation of cooling rates should be considered carefully.

E. Solidification

During rapid solidification of the weld pool, the undercooling of liquid metal is a critical parameter that controls the solidification microstructure and segregation effects. Since weld solidification proceeds from the preexisting solid substrate, only undercooling associated with growth is of importance, which is comprised of contributions from thermal, constitutional, kinetic, and solid curvature effects.[19] An accurate modeling of the weld pool solidification requires coupling of a sophisticated solidification model with the heat transfer and fluid model. In the present study, in order to simplify the calculations, no undercooling is considered. In other words, the equilibrium liquidus isotherm is assumed to

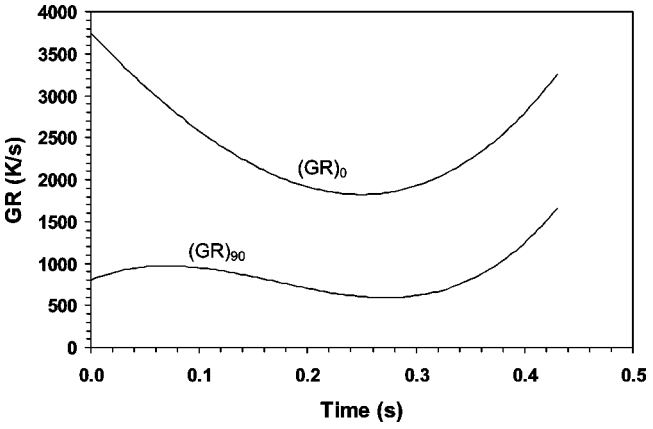

FIG. 15. Calculated solidification parameter GR at the 0° and 90° planes.

represent the liquid/mushy zone boundary, while the equilibrium solidus isotherm corresponds to the mushy zone/solid boundary. The solidification parameters presented in this work were calculated by considering only the heat transfer and fluid flow in the weld pool.

Figure 10 shows distances of the mushy zone/solid interface to the weld center, d_0 and d_{90}, as a function of the solidification time. The subscripts 0 and 90 are used to represent the value measured at the 0° and 90° planes, respectively, as shown in the figure. With the knowledge of the distance versus time data, the solidification rates, R_0 and R_{90}, are calculated as

$$R_0=\frac{d}{dt}(d_0), \quad R_{90}=\frac{d}{dt}(d_{90}). \tag{24}$$

Figure 11 shows the calculated solidification rates as a function of the solidification time at the 0° and 90° planes, where the peak temperature of the weld pool is superimposed. As shown in this figure, the solidification rates at both planes increase with time while the peak temperature decreases. The maximum solidification rate is reached when the peak temperature drops below the solidus temperature, i.e., the weld pool solidifies completely. The increasing solidification rate, which has been experimentally observed,[21] is reasonable on physical grounds. As shown in Fig. 12, a thin liquid shell with thickness of dr solidifies in a short time step dt. As dt approaches zero, we have $\lim_{dt\to 0}(A_S)=\lim_{dt\to 0}(A_L)=A$. Thus the heat balance equation is given as

$$A(k_S G_S-k_L G_L)dt=\overline{f_L}LAdr, \tag{25}$$

where A is the surface area of the thin shell, k_S and k_L are the thermal conductivity of solid and liquid, respectively, G_S and G_L are the temperature gradient in solid and mushy zone at the mushy zone/solid interface, respectively, and $\overline{f_L}$ is the average liquid fraction of the thin shell. It should be noted that the convective heat flux in the liquid is neglected in order to simply the discussion. Equation (25) can be rewritten as

$$R=\frac{dr}{dt}=\frac{k_S G_S-k_L G_L}{\overline{f_L}L}, \tag{26}$$

where R is the solidification rate. As shown in Fig. 6, G_L drops more rapidly than G_S during solidification. Furthermore, $\overline{f_L}$ decreases with time due to the release of the latent heat of fusion. As a result, the solidification rate increases with time.

The temperature gradients, G_0 and G_{90}, are evaluated in the mushy zone at the mushy/solid interface along the 0° and 90° planes, respectively. Figure 13 shows the plot of temperature gradients as a function of the solidification time. As shown in this figure, G_0 and G_{90} decrease with time.

The solidification rate, R, and temperature gradient, G, are important in the combined forms G/R and GR (cooling rate) as they can be related to the solidification morphology and the scale of the solidification substructure, respectively. Figure 14 depicts the solidification parameter G/R at the 0° and 90° planes. As shown in this figure, the solidification parameter G/R decreases, since G decreases while R increases with the solidification time. The maximum value of G/R is of the order of 10^2 K s/mm^2 at the 90° plane.

Using the solidification parameter G/R, the solidification front stability could be determined. The criterion for constitutional supercooling for plane front instability is given as[19]

$$G/R<\Delta T_E/D_L, \tag{27}$$

where ΔT_E is the equilibrium solidification temperature range at a given composition, and D_L is the solute diffusion coefficient in liquid. For 1005 steel, ΔT is equal to 23 K and D_L is taken as the carbon diffusion coefficient[22] in pure liquid iron, 2×10^{-2} mm^2/s. Thus $\Delta T/D_L$ is equal to 1.25×10^3 K s/mm^2 for 1005 steel. Therefore the plane front is unstable and the weld metal solidification microstructure will be of cellular or dendritic form.

The temporal variation of the solidification parameter G/R shown in Fig. 14 may result in changes in the solidification structures, since the interface morphology generally changes from cellular, cellular-dendritic to equiaxed-dendritic as the value of G/R decreases.[23] Thus we may expect a cellular type of microstructure close to the fusion line, an equiaxed-dendritic microstructure at the pool center, and a cellular-dendritic microstructure in between, during the solidification of the spot weld pool. It should be noted that the calculations presented here indicate aspects of solidification in a qualitative manner. Quantitative determination of the solidification microstructure requires not only the parameter G/R, but also the thermodynamics and kinetics of solidification.

The solidification parameter GR is useful to estimate the scale of the solidified substructure. Figure 15 shows the computed value of GR as a function of time at the two planes. Since G decreases and R increases with time, the parameter GR does not always change monotonically with time. Depending on how the rates of G and R change with time, the parameter GR can either increase or decrease with time. The average values of GR are 2500 and 900 K/s at the 0° and 90° planes, respectively.

It should be noted that the validation of the numerical model was limited to the weld pool geometry and cooling rates. The calculated solidification parameters have not been validated against the corresponding experimental results in 1005 steel spot welds, since the focus here was the examination of the results of the transient heat transfer and fluid flow model. However, the solidification parameters calculated using the transient model have been successfully used to predict the solidification structure in other alloy systems.[24] Furthermore, the solidification process investigated in the present model is governed only by the transfer of heat. An accurate prediction of the weld pool solidification will require consideration of both the thermodynamics and kinetics of solidification. In the future, a solidification model will be coupled with the transient thermofluid model to better understand the physics of solidification quantitatively.

V. CONCLUSIONS

The evolution of temperature and velocity fields during spot welding of 1005 steel was studied using a three-dimensional transient numerical model. The weld thermal cycles, weld pool geometry, and various solidification parameters could be quantitatively calculated. The following conclusions can be made from the investigation.

(1) The geometry of the FZ and HAZ and weld cooling curves predicted from the 3D transient heat transfer and fluid flow model were in good agreement with the corresponding experimental results. The calculated cooling rates are found to be almost independent of position between the 1073 and 773 K (800 and 500 °C) temperature range.

(2) Liquid metal convection is the dominant mechanism of heat transfer as the weld pool is fully developed, and thus determines the temperature distribution in the liquid pool and the pool shape. Heat transfer by conduction is important when the liquid velocity is small at the beginning stage of melting and during pool solidification.

(3) The size of the mushy zone, i.e., liquid+solid two phase region, grows significantly with time during solidification. This behavior can be explained from the heat transfer consideration taking into account the latent heat of fusion.

(4) The temperature gradients (G) in the mushy zone at the mushy zone/solid interface decrease with the solidification time. The solidification rate (R) of the mushy zone/solid interface increases with time as a result of the decrease of the temperature gradient and latent heat content in the unsolidified weld pool. The combination of solidification parameters G and R, i.e., G/R and GR, were quantitatively calculated and then used to estimate the solidification morphology and substructure in 1005 steel spot welds.

ACKNOWLEDGMENTS

The work was supported by a grant from the U.S. Department of Energy, Office of Basic Energy Sciences, Division of Materials Sciences, under Grant No. DE-FGO2-01ER45900. W. Z. gratefully acknowledges the award of a Fellowship from the American Welding Society. The authors would like to express their gratitude to Dr. Todd A. Palmer for performing the spot welding experiments.

[1] G. M. Oreper, J. Szekely, and T. W. Eager, Metall. Trans. B **17B**, 735 (1986).
[2] G. M. Oreper and J. Szekely, Metall. Trans. A **18A**, 1325 (1987).
[3] T. Zacharia, S. A. David, J. M. Vitek, and T. DebRoy, Weld. J. (Miami) **68**, 499s (1989).
[4] T. Zacharia, S. A. David, J. M. Vitek, and T. DebRoy, Weld. J. (Miami) **68**, 510s (1989).
[5] L. A. Betram, J. Eng. Mater. Technol. **115**, 24 (1993).
[6] W. H. Kim and S. J. Na, Int. J. Heat Mass Transf. **41**, 3213 (1998).
[7] Y. Wang and H. L. Tsai, Metall. Mater. Trans. B **32B**, 501 (2001).
[8] V. R. Voller and C. Prakash, Int. J. Heat Mass Transf. **30**, 2690 (1987).
[9] W. Pitscheneder, T. DebRoy, K. Mundra, and R. Ebner, Weld. J. (Miami) **75**, 71s (1996).
[10] S. V. Patankar, *Numerical Heat Transfer and Fluid Flow* (Hemisphere, New York, 1982).
[11] V. R. Voller and C. Prakash, Int. J. Heat Mass Transf. **30**, 1709 (1987).
[12] A. D. Brent, V. R. Voller, and K. J. Reid, Numer. Heat Transfer **13**, 297 (1988).
[13] K. Mundra, T. DebRoy, and K. M. Kelkar, Numer. Heat Transfer, Part A **29**, 115 (1996).
[14] S. Kou and D. K. Sun, Metall. Trans. A **16A**, 203 (1985).
[15] J. W. Elmer, J. Wong, and T. Ressler, Metall. Mater. Trans. A **32A**, 1175 (2001).
[16] W. Zhang, J. W. Elmer, and T. DebRoy, Mater. Sci. Eng., A **333**, 320 (2002).
[17] L. E. Samuels, *Light Microscopy of Carbon Steels* (ASM International, Materials Park, OH, 1999), p. 309.
[18] Z. Yang, Ph. D. thesis, The Pennsylvania State University, University Park, PA, 2000.
[19] T. DebRoy and S. A. David, Rev. Mod. Phys. **67**, 85 (1995).
[20] K. Mundra, T. DebRoy, S. S. Babu, and S. A. David, Weld. J. (Miami) **76**, 163s (1997).
[21] J. W. Elmer (private communication).
[22] W. Kurz and D. J. Fisher, *Fundamentals of Solidification* (Trans Tech, Switzerland, 1986).
[23] Ø. Grong, *Metallurgical Modeling of Welding*, 2nd ed. (The Institute of Materials, London, 1997), p. 256.
[24] S. S. Babu (private communication, Oak Ridge National Laboratory, 2002).